A Hybrid Data-Driven Power Loss Minimization Method of Dual-Active Bridge Converters

Ziheng Xiao, *Member, IEEE*, Yu Jiang, Zhigang Yao, Zhou He, *Graduate Student Member, IEEE*, Yongbin Jiang, *Member, IEEE*, Yaohua Li, and Yi Tang, *Senior Member, IEEE*

***Abstract*—Due to the intricate array of control parameters, achieving efficiency optimization for a typical dual active bridge (DAB) prototype becomes a laborious and time-intensive task. Traditional methodologies have revolved around an idealized lossless model of DAB, inevitably leading to a disparity between theoretical ideals and experimental realities. To surmount this challenge, we employ a hybrid data-driven model that seamlessly integrates insights derived from both simulation and experimentation. The disparity between the experimental and simulated models is represented as a residual branch, akin a nonlinear, and dissipative impedance. This residual branch contributes to a fraction of power losses and subsequent output voltage/power reduction. The strategic minimization of residual branch emerges as a pivotal step in identifying the optimal control parameters. These optimal control parameters are then subjected to practical testing on the DAB prototype, allowing for the evaluation of their effectiveness. By analyzing the results obtained from experiments conducted on a 3-kW DAB prototype, we leverage a perturbation-based optimal examination technique to validate the efficacy of the proposed efficiency optimization methodology.**

***Index Terms*—Data-driven model, dual active bridge converters, efficiency optimization.**

I. Introduction

THE dual active bridge (DAB) dc/dc converter, introduced in [1] and [2], consists of two full bridges connected by a power inductor and a high-frequency transformer (HFT). DAB continues to gain significant attention due to its numerous advantages, including galvanic isolation, zero-voltage switching-ON (ZVS), wide voltage gain range, high power density, and bidirectional power flow capability. These features have made DAB a popular choice for various applications, such as energy storage systems [3], [4], [5], microgrids [6], [7], [8], automation applications [9], [10], [11], and solid-state transformers [12], [13], [14].

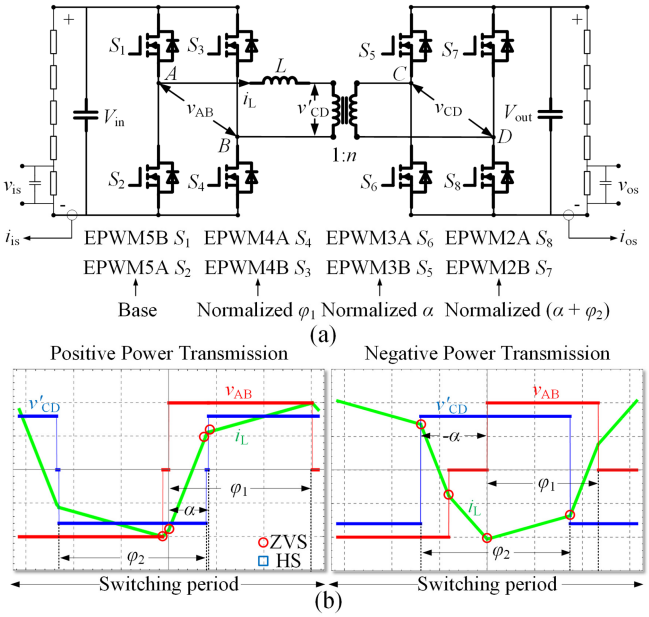

Fig. 1. (a) Topology of DAB. (b) Operating waveforms of DAB with positive and negative power transmission.

Fig. 1 depicts the power stage and the typical waveforms of fixed frequency symmetric modulated DAB. The DAB consists of four primary switches, four secondary switches, a power transmission inductor L and an HFT. The ratio of HFT is 1:n and the switching frequency is f_s. The output port voltage of AB and CD are v_{AB} and v_{CD}, and the inductor current is i_L. The power transmission, P of a DAB can be positive or negative by controlling the conducting sequences of the switches. The primary bridge pulse width angle φ_1, secondary bridge pulse width angle φ_2, and the phase shift angle α between two bridges are expressed in radian, respectively. The control parameter is expressed as $(\alpha, \varphi_1, \varphi_2)$. The range of α, φ_1, and φ_2 are $\alpha \in [-\pi, \pi]$, $\varphi_1 \in [0, \pi]$, and $\varphi_2 \in [0, \pi]$. The red circle, and blue square denote the switches are with ZVS, and hard switching.

DAB presents a spectrum of control freedoms, giving rise to the exploration of diverse modulation schemes aimed at bolstering its efficiency and power density. Within the realm of various

Manuscript received 11 November 2023; revised 15 January 2024; accepted 18 February 2024. Date of publication 22 February 2024; date of current version 20 March 2024. This work was supported by the National Natural Science Foundation of China under Grant 52107210. Recommended for publication by Associate Editor M. Scott. *(Corresponding author: Yi Tang.)*

Ziheng Xiao is with the Energy Research Institute, Nanyang Technological University, Singapore 639798 (e-mail: ziheng.xiao@ntu.edu.sg).

Yu Jiang is with the School of Electrical Engineering, Chinese University of Hong Kong, Hong Kong (e-mail: yujiang@cuhk.edu.hk).

Zhigang Yao is with the School of Electrical Engineering, Southwest Jiaotong University, Chengdu 610032, China, and also with the Energy Research Institute, Nanyang Technological University, Singapore 639798 (e-mail: zhigangyao@swjtu.edu.cn).

Zhou He is with the School of Electrical and Electronic Engineering, Huazhong University of Science and Technology, Wuhan 430074, China (e-mail: he_zhou@hust.edu.cn).

Yongbin Jiang, Yaohua Li, and Yi Tang are with the School of Electrical and Electronic Engineering, Nanyang Technological University, Singapore 639798 (e-mail: yongbin.jiang@ntu.edu.sg; yaohua001@e.ntu.edu.sg; yitang@ntu.edu.sg).

Color versions of one or more figures in this article are available at https://doi.org/10.1109/TPEL.2024.3368330.

Digital Object Identifier 10.1109/TPEL.2024.3368330

control approaches, single-phase shift (SPS) is widely adopted due to its simplicity [1], [2]. Nonetheless, SPS encounters a limitation in its ZVS range, leading to suboptimal efficiency when the voltage gain M significantly deviates from unity. To transcend this constraint and elevate DAB's performance, alternative control methodologies have emerged, including dual phase shift (DPS) [15], [16], [17], extended phase shift (EPS) [14], [18], [14], and triple phase shift (TPS) [19], [20], [21], [22]. These strategies are designed to curtail reverse current flow, peak current demand, and/or the root mean square (rms) current, thereby amplifying the overall efficiency of DAB. Most of the analyses centered on an idealized lossless model of DAB, disregarding its nonlinear characteristics and unconsidered parameters. Consequently, a disparity emerges between theoretical optima and experimental outcomes. The pioneering work of [23] identified disparities between the power flow under SPS modulation and analytical predictions. Subsequent studies [24], [25] delved into the influence of deadtime T_{d} on ZVS region and power transmission characteristics.

Owing to the intricate array of control parameters, achieving efficiency optimization for a typical DAB prototype becomes a laborious and time-intensive task. For instance, when contemplating a 30-step evenly distributed exploration of α, φ_1, and φ_2 to pinpoint the optimal efficiency point in one operating condition, an exhaustive $30^3 = 27\,000$ rounds of experiment efficiency measurements using a power analyzer become necessary, yet this magnitude of experimentation verges on impracticality. The challenge compounds further when the pursuit involves mapping out the optimal trajectory of control parameters across expansive operating conditions.

Recently, researchers have explored the application of artificial intelligence (AI) technologies in DAB optimization. Xiao et al. [26] employed transfer learning techniques to assess power loss and efficiency in power converters. Tang et al. [27] and Lin et al. [28] applied the Q-learning and data trimming methods, respectively, to augment the performance of DAB converters. However, it is noteworthy that both [27] and [28] relied exclusively on simulation data. This reliance poses a limitation, as the potential discrepancies between simulated outcomes and experimental results remain unaddressed. To address this challenge, we harness insights from both simulation and experimentation. To intricately capture the operational behavior of a DAB prototype, we establish an experimental data-driven power flow and voltage gain model through a high-speed automatic data acquisition platform. Concurrently, we conduct a parallel simulation utilizing a streamlined physical model.

The process flowchart of the proposed approach is illustrated in Fig. 2. Through data acquisition from both simulation and experimentation phases, a hybrid data-driven model is formed, integrating data-driven models derived from both simulated and experimental datasets. The disparity between the experimental and simulation models is represented as a residual branch. This residual branch can be envisioned as a nonlinear, dissipative impedance, contributing to a fraction of power losses and output voltage/power reduction. The minimization of this residual component becomes instrumental in the pursuit of identifying optimal control parameters. The optimal control parameters are then employed in testing on an experimental prototype to gauge their effectiveness. By analyzing the experimental outcomes, a perturbation-based optimal examination technique is employed to validate the proposed efficiency optimization methodology.

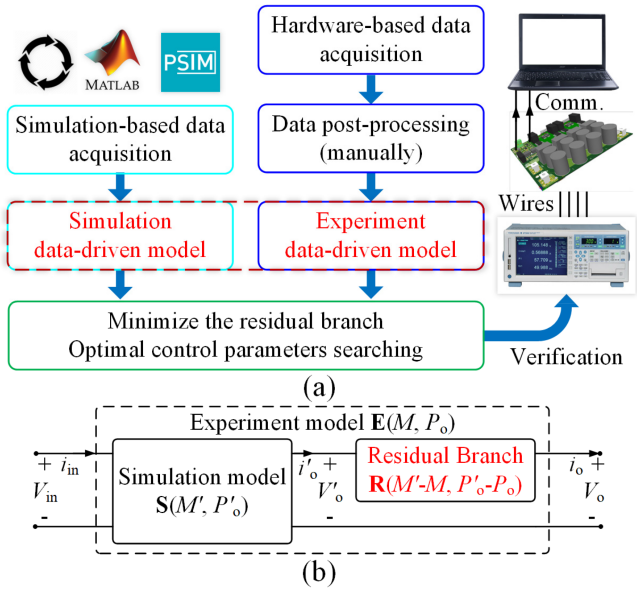

Fig. 2. (a) Flowchart of the proposed hybrid data-driven optimization method. (b) Relation between the M and P_{o} experiment data-driven model $\mathbf{E}(X, M, P_{\mathrm{o}})$, the M and P_{o} simulation data-driven model $\mathbf{S}(X, M', P'_{\mathrm{o}})$, and the residual branch $\mathbf{R}(X, M'\text{-}M, P'_{\mathrm{o}}\text{-}P_{\mathrm{o}})$.

The rest of this article is organized as follows. In Section II, the intricate procedure of the proposed method is expounded upon, encompassing the acquisition of both simulation and experiment data-driven models, alongside the optimization process for the residual branch. Section III presents the experimental results. Section IV presents the discussion. Finally, Section V concludes this article.

II. Hybrid Data-Driven Optimization Method

As depicted in Fig. 2, the proposed optimization method integrates both simulation and experimental parts. The method involves iterative collection of raw data through physical model simulations and hardware experiments. These combined datasets contribute to the construction of a hybrid data-driven model, encompassing information from both simulations and experiments. To address disparities between the simulation and experiment models, a residual branch is introduced.

The residual branch can be conceived as a nonlinear, dissipative impedance connected to a multitude of factors: the input voltage V_{in}, the load R_{L}, the phase shift angles (α, φ_1, φ_2), the deadtime T_{d}, the voltage gain M', and output power P'_{o} in the simulation part. The origin of this residual branch can be traced to disparities between the simulation model and the physical experimental prototype. Minimization of this residual branch facilitates the search for optimal control parameters [cf., Section II-C]. These optimized parameters are subsequently applied to an experimental prototype to assess their efficacy.

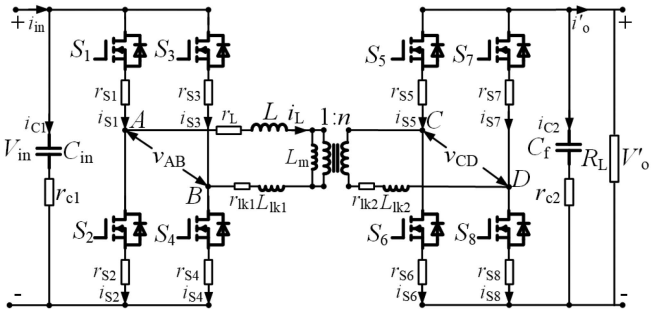

Fig. 3. Circuit diagram of DAB in the simulation process.

TABLE I
KEY VARIABLES IN THE SIMULATION PROCESS

Item	Values
(V_{inmin}, V_{inmax}, V_{instep}) V	(200, 360, 40)
(R_{Lmin}, R_{Lmax}, R_{Lstep}) Ω	(30, 110, 20)
(α_{min}, α_{max}, α_{step}) p.u.	(0.00, 0.50, 0.02)
(φ_{1min}, φ_{1max}, φ_{1step}) p.u.	(0.00, 1.00, 0.05)
(φ_{2min}, φ_{2max}, φ_{2step}) p.u.	(0.00, 1.00, 0.05)
(T_{dmin}, T_{dmax}, T_{dstep}) ns	(200, 400, 100)

A. Simulation Data-Driven Model

During the simulation phase, the circuit diagram for the DAB is presented in Fig. 3. The impedance analyzer is employed to measure the inductance L, and winding resistance r_L of the power inductor. Determination of the excitation inductance L_m, leakage inductance, and transformer resistances (L_{lk1}, L_{lk2}, r_{lk1}, r_{lk2}) involves measuring open/short circuit impedances using the impedance analyzer. Extracting information from their respective datasheets, the drain-source on-state resistance $r_{ds\text{-}ON}$ of the power MOSFETS r_{s1}–r_{s8}, and the equivalent series resistance of the two film capacitors (r_{c1}, r_{c2}) is achieved.

The circuit is subjected to iterative simulations involving four loops, namely the three phase shift angles (α, φ_1, φ_2), and the deadtime T_d. Maintaining a time step of 100 ns and a simulation duration of 20 ms ensures the circuit reaches a steady state. To ensure precision in results, the output voltage V'_o is computed by averaging across 10 switching cycles (2000 data points for $f_s = 50$ kHz). The values for V'_o and the voltage gain M' are expressed as follows:

$$V_o = \frac{1}{2000}\sum_{i=0}^{2000} V_{o-sim}(i) \tag{1}$$

$$M' = \frac{V_o}{nV_{in}} = \frac{1}{2000nV_{in}}\sum_{i=0}^{2000} V_{o-sim}(i) \tag{2}$$

$$P'_o = \frac{V_o^2}{R_L} = \frac{n^2V_{in}^2M'^2}{R_L}. \tag{3}$$

Table I provides a comprehensive summary of the initial values, final values, and iteration steps for all variables during the simulation phase. In total, an extensive set of simulations amounting to $5\times5\times21\times21\times26\times3 = 859950$ samples was conducted. This vast collection results from the permutations of

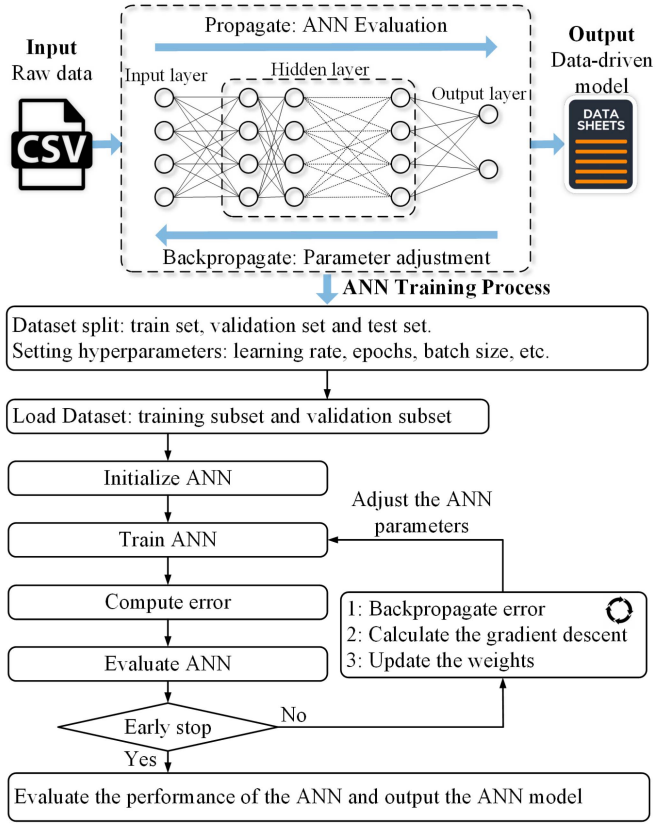

Fig. 4. Training process of the ANN (the input is the raw data, and the output is the data-driven model after the training process).

input variables (V_{in}, R_L, α, φ_1, φ_2, T_d) and output variables (V'_o, M'). A simple feedforward artificial neuron network (ANN) is utilized to determine the optimal nonlinear fitting for the following pair of equations:

$$M' = f_1(\alpha, \varphi_1, \varphi_2, T_d, V_{in}, R_L) \rightarrow f_1(x_1; \theta_1) \tag{4}$$

$$P'_o = f_2(\alpha, \varphi_1, \varphi_2, T_d, V_{in}, R_L) \rightarrow f_2(x_1; \theta_2) \tag{5}$$

where x_1 denotes the input variables, θ_1 and θ_2 correspond to the ANN hyperparameters learned from the data.

The design process of the feedforward ANN hinges on two pivotal factors: network size and accuracy. Enhanced accuracy can be attained by augmenting the count of neurons and layers within the network. As depicted in Fig. 4, the ANN acquires knowledge from data through the training algorithm. To address the regression problem at hand, quadratic loss functions have been employed for solution, as outlined in the following equations:

$$L_1(M', f_1(x_1;\theta_1)) = (M' - f_1(x_1;\theta_1))^2 \tag{6}$$

$$L_2(P'_o, f_2(x_1;\theta_2)) = (P'_o - f_2(x_1;\theta_2))^2. \tag{7}$$

Throughout the training process, the weights and parameters of the ANN undergo adjustments of θ_1 and θ_2. These values are attained through optimization techniques aimed at minimizing

TABLE II
SPECIFICATIONS OF THE EXPERIMENTAL PROTOTYPE

Component	Part number	Parameters
MOSFETs	C3M0021120K	1.2-kV, 21-mΩ
MCU	TMS320F28377D	Digital signal processer C2000 32-bit 200-MHz
Input and output electrolytic cap.	EKXG401ELL330ML20S two in series	33-μF, 400-V, 0.24 dissipation factor.
Input and output film cap.	F862BZ564K310ZV054 two in series	560-nF, 560-V,0.03 dissipation factor.
Power inductor	Magnetics Kool Mμ core part number 77440	2 cores in parallel, 46 μH at 50 kHz
Inductor wires	400 strands Litz wire	21 turns, 13 mΩ, d_r = 100 μm.
HFTs	12T/18T, EE70 core 600 strands Litz wire	$L_{lk} \approx 2.7$-μH, $L_m \approx 597$-μH.

the loss functions

$$\theta_1 = \arg\min_{\theta_1} L_1\left(M', f_1\left(x_1;\theta_1\right)\right) \tag{8}$$

$$\theta_2 = \arg\min_{\theta_2} L_2\left(P'_{\mathrm{o}}, f_2\left(x_1;\theta_2\right)\right). \tag{9}$$

The training process operates in an iterative manner. Initially, the connections between neurons across the input, hidden, and output layers of the ANN are initialized with random weights. Normalization is applied to both input and output data to ensure uniform processing. Subsequently, the input data is introduced into the ANN, triggering a forward propagation of signals that culminates in generating an output. Discrepancies between the predicted output and the actual output are computed as errors. For enhancing the ANN's performance, the backpropagation algorithm employs the gradient descent technique to iteratively adjust the weights. This sequence is reiterated until the error diminishes to an acceptable level, signifying the successful completion of the training process.

B. Experimental Data-Driven Model

There are two steps to obtain the experiment data-driven model. 1) Hardware-based high speed automatic data acquisition. 2) Software-based ANN design and training.

1) High Speed Automatic Data Acquisition Method: A solid foundation for data-driven modeling methods is established by a large-scale and high-quality database, which significantly affects the accuracy of the models. Therefore, there is a need for a high-speed automated data acquisition method. Increasing the level of automation also mitigates errors arising from human factors during the measurement process. Fig. 5 depicts the testbed for automatic data acquisition, while Table II provides an overview of the electrical parameters associated with the DAB. Before conducting the test, several factors need to be determined. 1) The range and iteration step for all the control parameters. 2) The sampling rate and data acquisition speed. 3) Data qualities and error.

The maximum transition time in the worst case was less than 5 ms. To provide some margin and ensure accurate measurements, we opted for a 10 ms interval between two consecutive measurements. The input and output voltages are sampled using

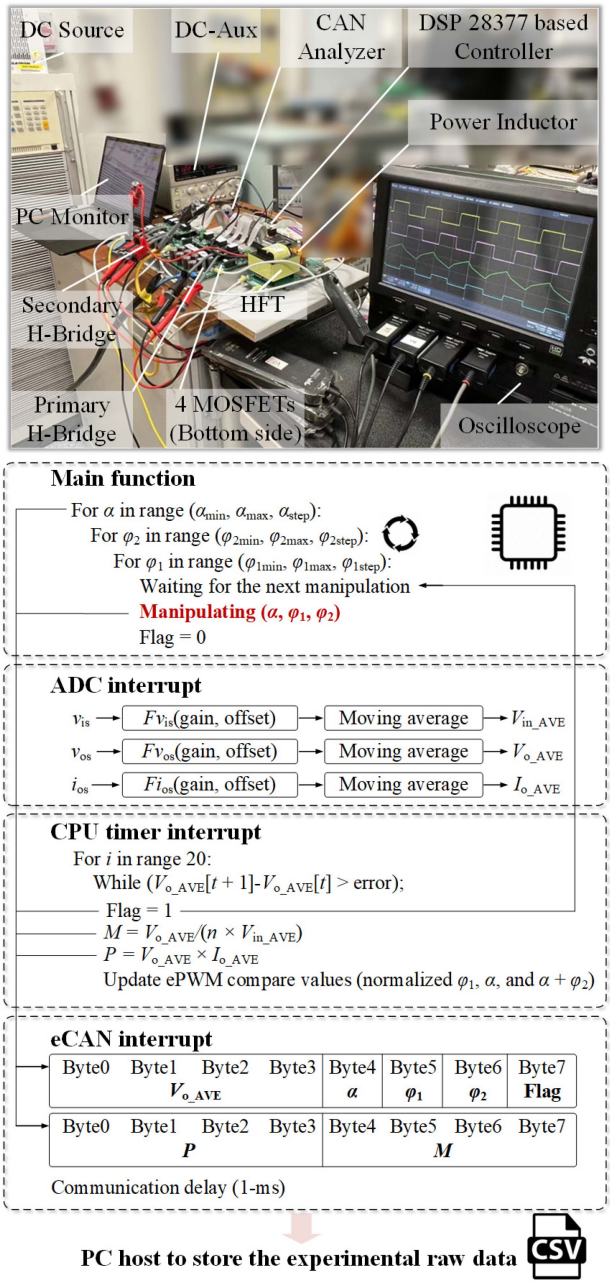

Fig. 5. Experimental testbed and the implemented algorithm for the automatic data acquisition platform.

a resistor divider circuit, while the input and output currents are sampled using a high precision low temperature drift shunt resistor. The sampled voltages and currents are denoted as v_{is}, i_{is}, v_{os}, and i_{os}, respectively. To effectively filter out switching-level noise without introducing substantial phase lag, the cutoff frequencies of the sampled voltage and current signals are set at 10 and 20 kHz, respectively. The signals are transmitted to the inner analog-to-digital converter (ADC) of the DSP through a signal conditioning circuit. The DAB comprises four phase legs, with the power MOSFETS being controlled by four enhanced PWM (ePWM) controllers labeled as EPWM5 to EPWM2. EPWM5 is designated as the base controller, while the phase differences

of EPWM4, EPWM3, and EPWM2 represent the normalized values of φ_1, α, and $(\alpha + \varphi_2)$. This configuration aligns with the operational waveform depicted in Fig. 1, corresponding to the experimental setup.

The sweeping control algorithm is illustrated at the bottom of Fig. 5. Regarding the ADC interrupt, the values of $v_{\rm is}$, $v_{\rm os}$, and $i_{\rm os}$, are converted to their corresponding actual values of $V_{\rm in}$, $V_{\rm o}$, and $I_{\rm o}$ through three affine functions. The gains and offsets are determined via the calibration test. The gains and offsets for these conversions are determined through the calibration test. Additionally, a four-bit moving averaging function is applied to ensure smoothness in the sampled signals. The ADC sampling interrupt is triggered by the pulse width modulation (PWM) switching signal, resulting in the sampling frequency being equal to the switching frequency.

A CPU timer is employed to capture the electrical information during the steady state. The interrupt frequency for this timer is set to 10 ms to ensure the availability of every steady state data. Once the output voltage ripple falls below a predefined error (3% fluctuation in this iterative data acquisition method), the voltage gain M and output power P under this condition are calculated. All the electrical information is then transmitted from the DSP to a PC host using a control area network analyzer. To transmit the measurement results, two frames are utilized for each measurement.

For all the three phase shift angles, we selected an iteration step of 0.02-p.u. As a result, there are a total of $51 \times 51 \times 101 = 262\,701$ iterations required to traverse all the control parameters. Using this system, the entire process of traversing all the control parameters takes approximately 50 min, without the need for any human intervention. Please note that these measurements were taken under a fixed selection of $V_{\rm in}$, R, $f_{\rm s}$, and $T_{\rm d}$. Multiple sweeping tests would be required to gather the necessary data in different operating conditions.

The quality of the data plays a crucial role in the performance of the data-driven method. The error in the measurements can stem from various factors, such as the resolution limitations of the inner ADC of the DSP, quantization noise, electrical noise during testing, and others. To ensure accurate measurements, calibration experiments were conducted by comparing the ADC readings against a digital multimeter. The relative error for both input and output voltages were 0.96%. The input and output dc currents were also calibrated, yielding an error of 0.56%. Consequently, the maximum error in voltage gain is –1.8% to 1.9%, and the maximum error in output power is –1.5% to 1.5%. The application of a 4-bit moving average during the sampling process helps minimize and keep the error within acceptable limits.

Data postprocessing is necessary before feeding it into the ANN. During the analysis of the original data, it was observed that in certain operating conditions, the output voltage is negative (around –3 V), which could be attributed to voltage drops across the secondary power MOSFETS. Additionally, abnormal behavior was noticed in the sampled output voltage and current when φ_1, α, and $(\alpha + \varphi_2)$ are close to the 0 or π. Moreover, when α, φ_1, and φ_2 fall within the predefined iterative range, the changes in M and P are not consistently smooth when the three control parameters are altered in one iteration. To address these issues, any data generated during the abnormal conditions are manually discarded. The data size for one case amounts to approximately 180 000 after this process.

TABLE III
ERROR PROBABILITY DISTRIBUTION SUMMARY

	Error of M in ANN	Analytical	Error of P in ANN	Analytical
Mean	-1.64E-04	1.91E-01	2.47E-05	6.50E-02
Maximum	5.50E-01	2.15E+00	3.12E-01	8.24E-01
standard deviation	1.40E-02	5.88E-01	4.65E-03	1.75E-01
3σ region (lower)	-4.20E-02	-1.57E+00	-1.39E-02	-4.61E-01
3σ region (upper)	-6.56E-04	7.65E-01	9.87E-05	2.60E-01

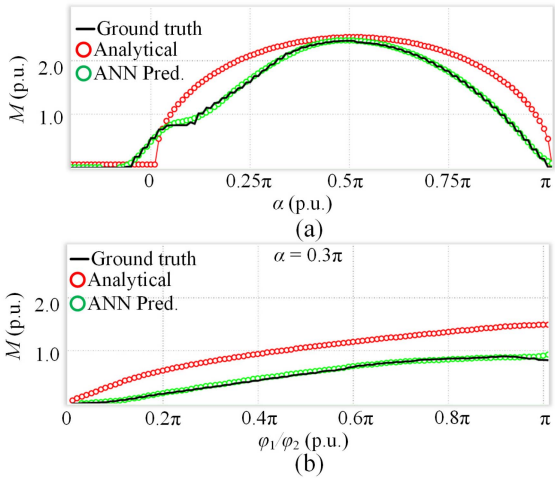

Fig. 6. Curves of the measured ground truth, the analytical calculation, and the ANN perdition in. (a) SPS scenario. (b) DPS scenario.

During this process, we choose $V_{\rm in} = 240$ V, $f_{\rm s} = 50$ kHz, R is changed from 50 to 100 Ω with 10 Ω iteration step, and the default value of $T_{\rm d}$ is 300 ns (0.03 p.u.).

2) ANN Design and Training: To prepare the data for training, the original dataset is shuffled, and then split into three sets: 70% for training, 10% for validation, and 20% for testing. We executed the training process on a personal computer with an Intel Core i7-3770 CPU and 8 GB RAM, and the training process for the ANN with 256 neurons took approximately 2 h to complete.

Table III summarized the errors for the voltage gain M prediction in analytical method as well as the ANN methods. The error of voltage gain M is calculated as

$$M_{\rm Error} = \frac{M_{\rm Prediction} - M_{\rm Measure}}{M_{\rm Measure}}. \tag{10}$$

Fig. 6 illustrates the curve of the measured ground truth, along with the curves obtained using various prediction methods. In SPS where α is close to 0.5π, the analytical method is close to the ground truth. When α is away from 0.5π, the error of the analytical method increases. There are some interesting phenomena in this case. 1) Theoretically, there should be no

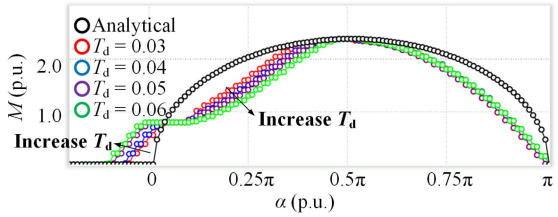

Fig. 7. Deadtime impact on the power flow and voltage gain of a DAB in SPS scenario.

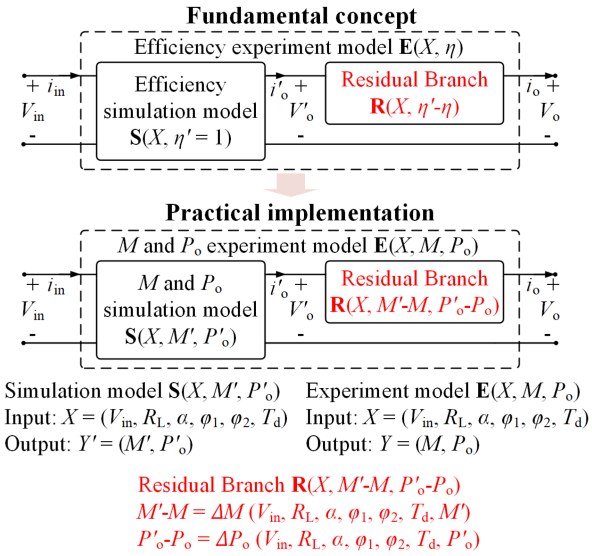

Fig. 8. Fundamental concept and practical implementation of the proposed method. In the fundamental concept part, the residual branch $\mathbf{R}(X, \eta'\text{-}\eta)$ is modeled as the discrepancy between the efficiency experiment model $\mathbf{E}(X, \eta)$, and the efficiency simulation model $\mathbf{S}(X, \eta' = 1)$. In the practical implementation part, the residual branch $\mathbf{R}(X, M'\text{-}M, P'_o\text{-}P_o)$ is modeled as the discrepancy between the M and P_o experiment model $\mathbf{E}(X, M, P_o)$ and the M and P_o simulation model $\mathbf{S}(X, M', P'_o)$.

power transmission when $\alpha < 0$ in the analytical method, but the effective power transmission range can be extended to $\alpha < 0$. 2) In some regions when $0 < \alpha < 0.1\pi$, the power transmission and voltage gain is almost unchanged with the change of α. Fig. 6(b) illustrates the curves corresponding to DPS. It can be observed that the actual values of P and M tend to be smaller compared to those obtained from the analytical method.

We also investigated the impact of deadtime T_d on the voltage gain M, and the results in SPS is depicted in Fig. 7. When D_t increases, M decrease under identical control parameters when $\alpha < 0.5\pi$. Additionally, a larger T_d also extends the range of power transmission to negative α values.

C. Optimization of the Residual Branch

The fundamental concept and practical implementation of our proposed method are illustrated in Fig. 8. To begin, let's assume we have acquired efficiency models for both the simulation model, denoted as $\mathbf{S}(X, \eta')$, and the experimental model, denoted as $\mathbf{E}(X, \eta)$, where $X = (V_{in}, R_L, \alpha, \varphi_1, \varphi_2, T_d)$ represents the operating conditions and control parameters. For simplicity, we have employed an ideal simulation model, which sets the efficiency in the simulation model to $\eta' = 1$. The residual branch, $\mathbf{R}(X, \eta'\text{-}\eta)$, can be interpreted as the efficiency drop or power loss, as it is connected in series at the output side of $\mathbf{S}(X, \eta')$. From a data-driven modeling perspective, $\mathbf{R}(X, \eta'\text{-}\eta)$ signifies the deviation between $\mathbf{S}(X, \eta')$ and $\mathbf{E}(X, \eta)$. Minimizing $\eta'\text{-}\eta$ within $\mathbf{R}(X, \eta'\text{-}\eta)$ leads to the lowest power loss and maximum efficiency. However, acquiring sufficient experimental data for the experiment data-driven model process, by measuring the prototype's efficiency with a power analyzer, proves tedious, and time-consuming. Consequently, the efficiency model in the initial concept is modified to the M and P_o experiment model in the implementation phase.

The input parameters for both the simulation model, $\mathbf{S}(X, M', P'_o)$, and the experimental model, $\mathbf{E}(X, M, P_o)$, are represented by $X = (V_{in}, R_L, \alpha, \varphi_1, \varphi_2, T_d)$. The output parameters for $\mathbf{S}(X, M', P'_o)$ and $\mathbf{E}(X, M, P_o)$ are $Y' = (M', P'_o)$ and $Y = (M, P_o)$, respectively. The residual branch, $\mathbf{R}(X, M'\text{-}M, P'_o\text{-}P_o)$, is recognized as the output voltage/power reduction. At each operating point where M and P_o are predefined, the difference between M and P_o in the simulation and experiment is referred to as

$$M' - M = \Delta M\left(V_{in}, R_L, \alpha, \varphi_1, \varphi_2, T_d, M'\right) \tag{11}$$

$$P'_o - P_o = \Delta P\left(V_{in}, R_L, \alpha, \varphi_1, \varphi_2, T_d, P'_o\right). \tag{12}$$

Given that (X, Y) and (X, Y') encompass both the control parameters $x = (\alpha, \varphi_1, \varphi_2, T_d)$ and the operating condition $z = (V_{in}, R_L, M, P_o)$, the objective of optimization is to identify the optimal control parameters, denoted as $x_{opt} = (\alpha_{opt}, \varphi_{1opt}, \varphi_{2opt}, T_{dopt})$ when the operating condition z is given. In simpler terms, the pursuit of minimizing power loss can be equated to optimizing the residual branch to minimize discrepancies, denoted as ΔM and ΔP, in relation to given reference values of M and P_o (M_{ref}, P_{ref}).

Mathematically, this problem can be written as

$$\begin{aligned} &\text{Minimize } L\left(x, z; \theta\right) = c_1(\Delta P)^2 + c_2(\Delta M)^2 \\ &\text{subject to } \begin{cases} M_{ref} = M\left(V_{in}, R_L, \alpha, \varphi_1, \varphi_2, T_d\right) \\ P_{ref} = P_o\left(V_{in}, R_L, \alpha, \varphi_1, \varphi_2, T_d\right) \end{cases} \end{aligned} \tag{13}$$

where $\theta = (\theta_1, \theta_2)$ denotes the already learnt ANN hyperparameters of the hybrid data-driven model. $c_1 = 1/3$, $c_2 = 2/3$ are the normalized coefficients to ensure ΔM and ΔP share a similar contribution factor. This choice is made because during one of the control parameter sweeps in the experimental data-driven approach, a constant resistor load was employed, resulting in a relationship where $P_o \propto M^2$. Consequently, we opt to utilize $c_2 = 2c_1$ in this specific scenario.

The optimal control parameters obtained from the optimization process is given as

$$x_{opt} = (\alpha_{opt}, \varphi_{1opt}, \varphi_{2opt}, T_{dopt}) = \arg\min_x L\left(x, z; \theta\right). \tag{14}$$

Fig. 9 illustrates the three-dimensional density plots of $L(x, z; \theta)$ under different conditions. Within these scenarios, the nadir of $L(x, z; \theta)$ is represented as $L_{min}(x, z; \theta)$, sought through the application of the gradient descent method. It is discernible from

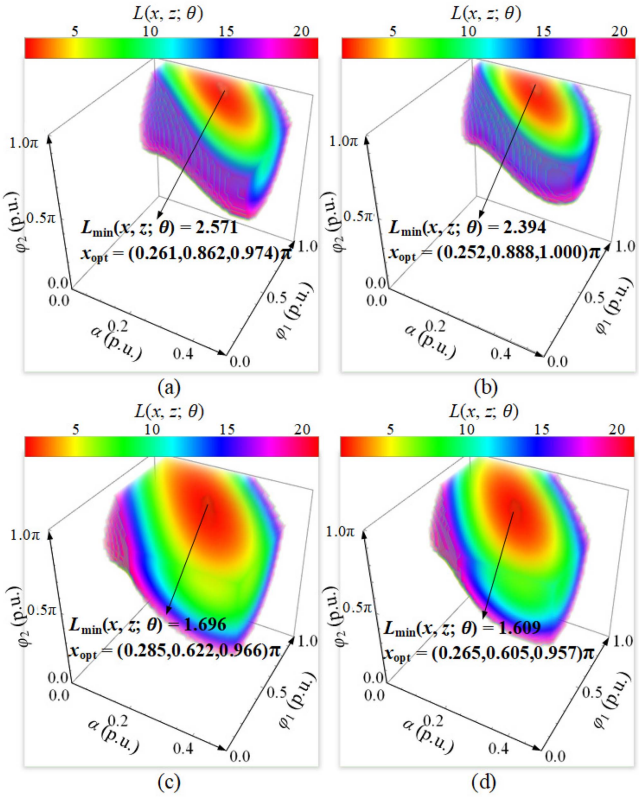

Fig. 9. Three-dimensional density plots of $L(x, z; \theta)$ under different conditions. (a) $M = 0.6$, $P = 0.35$, $T_d = 300$ ns. (b) $M = 0.6$, $P = 0.35$, $T_d = 200$ ns. (c) $M = 0.8$, $P = 0.5$, $T_d = 300$ ns. (d) $M = 0.8$, $P = 0.5$, $T_d = 200$ ns.

Fig. 9 that a reduced T_d leads to a decrease in the value of $L(x, z; \theta)$, signifying heightened efficiency. It should be noted that $L(x, z; \theta)$ in different conditions correlate not only with the efficiency of the DAB converter under different operating conditions, but also with the model discrepancies between the simulation-driven and experimental data-driven models. An increased discrepancy in electrical parameters between the simulation model and the experimental prototype correlates with an elevation in $L(x, z; \theta)$ across different operational conditions. However, this variation does not significantly impede the process of identifying $L_{min}(x, z; \theta)$.

The procedure for identifying x_{opt} is detailed in Fig. 10. Employing a four-variable iterative loop, we implement a "Beat the Top" algorithm to ascertain x_{opt}. In this algorithm, $z = (V_{in}, R_L, M, P_o)$ functions as the input variable, while $x_{opt} = (\alpha_{opt}, \varphi_{1opt}, \varphi_{2opt}, T_{dopt})$ serves as the output variable. After obtaining x_{opt} in different operating conditions, we used a single layer 32-neuron ANN to fit α_{opt}, φ_{1opt}, φ_{2opt}, and T_{dopt}. The calculated (optimal searching) results as well as the ANN fitted results are depicted in Fig. 11. It is imperative to emphasize that the scope of data collected during the data acquisition phase ought to be more extensive than the range applied in the implementation phase. This strategy ensures that the operational point invariably resides within the ambit of the fitted range across all conceivable scenarios. This fitted ANN for prediction the optimal control parameters is loaded into the controller for real-time calculation and implementation.

```
Opt. searching (V_in, R_L, M, P_o) {
  L = 100000
  for α in range (α_min, α_max, α_step):
    for φ1 in range (φ1min, φ1max, φ1step):
      for φ2 in range (φ2min, φ2max, φ2step):
        for T_d in range (T_dmin, T_dmax, T_dstep):
          x = (α, φ1, φ2, T_d)
          if( L(x, z; θ) < L)
              L = L(x, z; θ);
              α_opt = α; φ1opt = φ1; φ2opt = φ2; T_dopt = T_d;
          end
  Return (α_opt, φ1opt, φ2opt, T_dopt)}
```

Fig. 10. "Beat the Top" algorithm of search for x_{opt}.

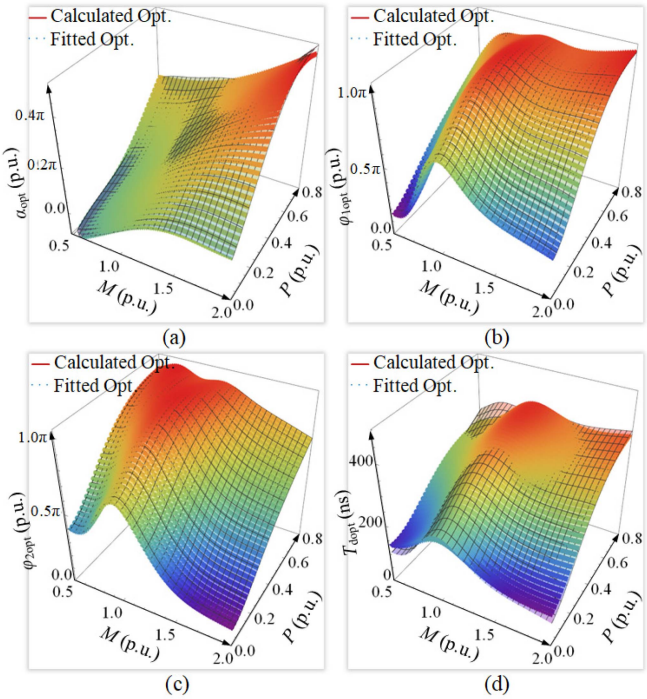

Fig. 11. Calculated and ANN fitted trajectory of x_{opt} in different operating conditions. (a) Trajectory of α_{opt}. (b) Trajectory of φ_{1opt}. (c) Trajectory of φ_{2opt}. (d) Trajectory of T_{dopt}.

III. Experimental Result

The experimental waveforms for sweeping the three phase shift angles are presented in Fig. 12. Each φ_1 loop takes approximately 610 ms, and once the φ_2 loop concludes, α increases by α_{step} while φ_2 begins from zero.

The control diagram of this method is depicted in Fig. 13. After determining the optimal control reference values (α_{opt}, φ_{1opt}, φ_{2opt}, T_{dopt}), a low-pass filter with a 200-Hz cutoff frequency is implemented to attenuate abrupt fluctuations in the control parameters. Because α_{opt} is more sensitive to the output voltage and power transmission, α_{opt} is utilized as the control variable in closed-loop control systems. In contrast, φ_{1opt}, φ_{2opt}, and T_{dopt} are calculated from the sampled electrical signals. Afterward, the values in the EPWM registers from

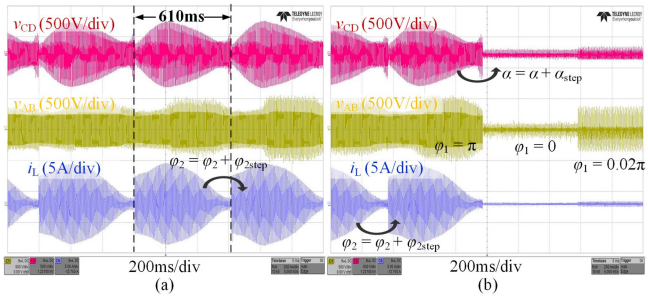

Fig. 12. Experimental waveforms for sweeping the three phase shift angles. (a) Inner φ_1 and φ_2 loop process. (b) Outer α loop process.

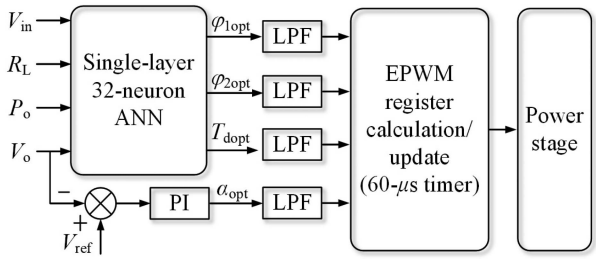

Fig. 13. Diagram of the deployed control algorithm.

EPWM2 to EPWM5 are updated to reflect these parameters. The proposed methodology requires an execution time of 54 μs to ascertain the optimal control parameters. Therefore, a control cycle duration of 60 μs has been selected, with updates to the EPWM registers occurring every three control cycles.

To evaluate the effectiveness of various methods, we conducted three distinct experimental comparisons. The waveforms of these three cases are depicted from Figs. 14–16. During these experimental trials, a consistent input voltage of $V_{in} = 240$ V was applied. The load resistance was adjusted to accommodate diverse output power conditions. The resulting M and output power p_o for these three scenarios are as follows: Case 1: $M = 0.6$, $p_o = 1.2$ kW ($P_o = 0.7$), Case 2: $M = 1.4$, $p_o = 0.79$ kW ($P_o = 0.2$), and Case 3: $M = 1.4$, $p_o = 2.4$ kW ($P_o = 0.6$). x_{opt} in these three cases are $x_{opt} = (0.113, 0.632, 1.000)\pi$, $T_d = 225$ ns, $x_{opt} = (0.234, 0.884, 0.586)\pi$, $T_d = 204$ ns, and $x_{opt} = (0.310, 1.000, 0.785)\ \pi$, $T_d = 188$ ns, respectively.

In Case 1 when the control parameter is away from x_{opt}, both the peak and rms current increases, leading to a reduction in efficiency. This effect is mitigated due to a relatively high output power with $P_o = 0.7$ in this scenario, which minimizes the noticeable differences in efficiency among varying control parameters. Moving on to Case 2, the proposed control parameters successfully achieve ZVS for all power MOSFETS. Conversely, the minimum rms current method, as well as the SPS method, exhibit evident switching spikes. Comparable observations can also be made in Case 3. Furthermore, when a longer T_d is implemented in Fig. 16(c), even though the waveforms maintain a semblance of similarity, there is still a discernible drop in efficiency when compared in the context of Fig. 16(b).

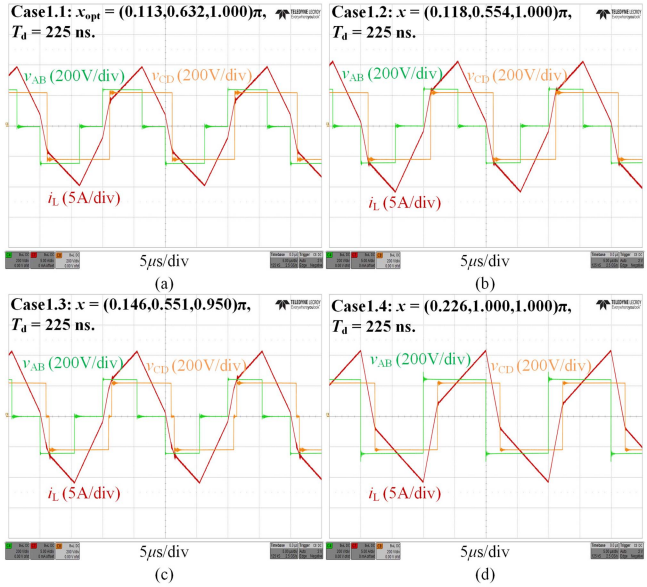

Fig. 14. Experimental waveforms in case1. (a) Case1.1: $x_{opt} = (0.113, 0.632, 1.000)\pi$, $T_d = 225$ ns. (b) Case1.2: $x = (0.118, 0.554, 1.000)\pi$, $T_d = 225$ ns. (c) Case1.3: $x = (0.146, 0.551, 0.950)\pi$, $T_d = 225$ ns. (d) Case1.4: $x = (0.226, 1.000, 1.000)\pi$, $T_d = 225$ ns.

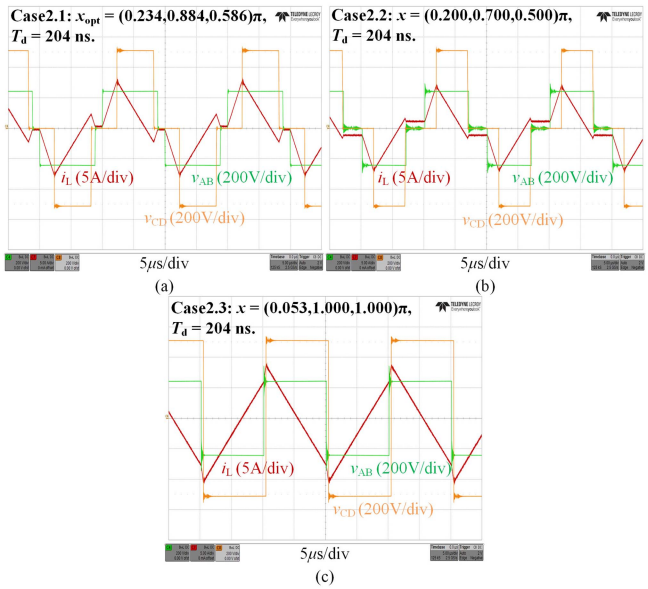

Fig. 15. Experimental waveforms in case2. (a) Case2.1: $x_{opt} = (0.234, 0.884, 0.586)\pi$, $T_d = 204$ ns. (b) Case2.2: the minimum rms current method, $x = (0.200, 0.700, 0.500)\pi$, $T_d = 204$ ns. (c) Case2.3: the SPS control method, $x = (0.053, 1.000, 1.000)\pi$, $T_d = 204$ ns.

We introduced a slight perturbation (Δx_{opt}) to the optimal control parameter x_{opt} to assess the attainment of the efficiency-optimal point. The perturbation is given as

$$\Delta x_{opt}\,|\Delta\alpha = (\Delta\alpha/\alpha_{opt}, \varphi_{1opt}, \varphi_{2opt}, T_{dopt}) \quad (15)$$

$$\Delta x_{opt}\,|\Delta\varphi_1 = (\alpha_{opt}, \Delta\varphi_1/\varphi_{1opt}, \varphi_{2opt}, T_{dopt}) \quad (16)$$

$$\Delta x_{opt}\,|\Delta\varphi_2 = (\alpha_{opt}, \varphi_{1opt}, \Delta\varphi_2/\varphi_{2opt}, T_{dopt}) \quad (17)$$

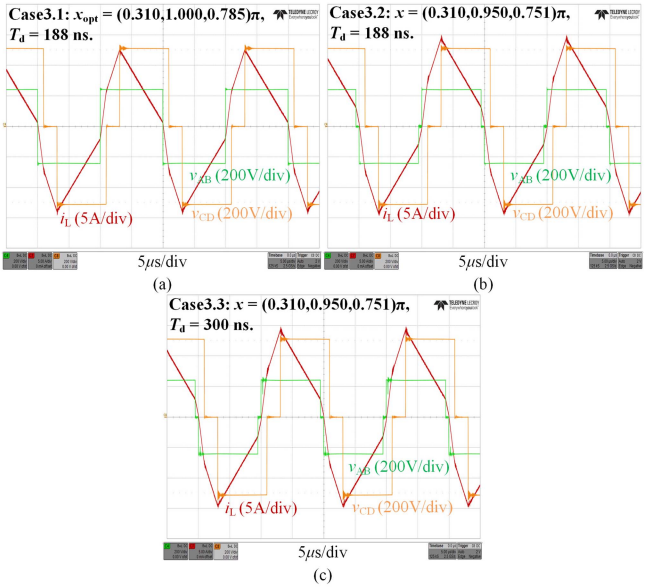

Fig. 16. Experimental waveforms in case3. (a) Case3.1: $x_{\mathrm{opt}} = (0.310, 1.000, 0.785)\pi$, $T_{\mathrm{d}} = 188$ ns. (b) Case3.2: $x = (0.310, 0.950, 0.751)\pi$, $T_{\mathrm{d}} = 188$ ns. (c) Case3.3: $x = (0.310, 0.950, 0.751)\pi$, $T_{\mathrm{d}} = 300$ ns.

$$\Delta x_{\mathrm{opt}}\left|\Delta T_{\mathrm{d}}\right. = \left(\alpha_{\mathrm{opt}}, \varphi_{1\mathrm{opt}}, \varphi_{2\mathrm{opt}}, \Delta T_{\mathrm{d}}/T_{\mathrm{dopt}}\right). \tag{18}$$

The efficiency drop after perturbation is given as

$$\Delta\eta\left(\Delta x_{\mathrm{opt}}\right) = \eta\left(x_{\mathrm{opt}}\right) - \eta\left(x_{\mathrm{opt}} + \Delta x_{\mathrm{opt}}\right). \tag{19}$$

Consider a maximum perturbation of 30%, the maximum efficiency drop, $\Delta\eta(0.3)$ is given as

$$\begin{aligned}&\Delta\eta\left(0.3\right) = \max\left(\Delta\eta\left(\Delta x_{\mathrm{opt}}\right)\right)\\ &\text{subject to}\\ &\left|\Delta\alpha\right| \le 0.3 \wedge \left|\Delta\varphi_1\right| \le 0.3 \wedge \left|\Delta\varphi_2\right| \le 0.3 \wedge \left|\Delta T_{\mathrm{d}}\right| \le 0.3.\end{aligned} \tag{20}$$

The outcomes of this investigation are presented in Fig. 17. Notably, it can be observed that as the magnitude of $|\Delta x_{\mathrm{opt}}|$ increases in either direction, the efficiency η experiences a reduction. This trend confirms the successful achievement of the efficiency-optimal point through the proposed method.

Drawing conclusions from the insights provided by Fig. 16, the following observations are made.

1) In the context of positive Δx_{opt} conditions, the influence of T_{d} is relatively subdued when compared to the impact of the three phase shift angles. This implies that by maintaining an adequate margin in T_{d}, the decline in efficiency is not substantial, particularly in scenarios involving high power conditions.
2) In contrast to the effects of φ_1 and φ_2, the impact of α is more pronounced.
3) The discrepancy in efficiency ($\Delta\eta$) in high power conditions is smaller than that observed in low power conditions. This suggests that, regardless of the control method employed, the efficiencies of the DAB exhibit greater similarity in high power conditions.
4) Upon introducing a negative Δx_{opt} adjustment to T_{d}, a clear drop in efficiency is evident when ΔT_{dopt} surpasses –15%. This points to the loss of ZVS capability in the DAB due to inadequate T_{d}, leading to a substantial efficiency reduction, particularly in low power conditions.

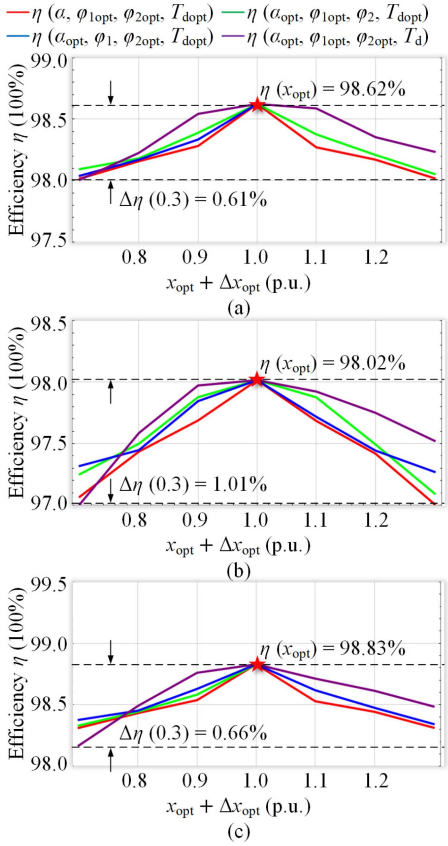

Fig. 17. Efficiency of the DAB prototype when applied a slight perturbation Δx_{opt} to the optimal parameter values x_{opt}. (a) Case1. (b) Case2. (c) Case3.

The efficiency curves for the DAB prototype under two different output voltage conditions are shown in Fig. 18. These conditions correspond to input voltage $V_{\mathrm{in}} = 240$ V, with output voltages of $V_{\mathrm{o}} = 504$ V ($M = 1.4$), and $V_{\mathrm{o}} = 216$ V ($M = 0.6$), respectively. The output power and the corresponding control parameters can be adjusted through changes in the load resistance. Distinct control methods are illustrated by the red, blue, orange, and purple lines. These lines correspond to the SPS modulation scheme [1], [2], the DPS modulation scheme [15], [16], [17], the minimum I_{rms} modulation scheme [20], [21], [22], and the proposed optimal control parameter, respectively.

In Fig. 18(a), the highest efficiency, at 98.62%, is achieved when $p_{\mathrm{o}} = 1.8$ kW ($P_{\mathrm{o}} = 0.45$). However, when the power is increased to 3.0 kW, the efficiency experiences a slight reduction to 98.33%. Under lighter load conditions, specifically when $p_{\mathrm{o}} = 0.12$ kW ($P_{\mathrm{o}} = 0.03$), the SPS modulation scheme demonstrates an efficiency of 94.21%, whereas the proposed optimal control parameter method maintains a notably high efficiency of 98.05%. Similar trends in efficiency can be observed when the output voltage is reduced to 216 V ($M = 0.6$). In Fig. 17(b), the peak efficiency is 98.43% at $p_{\mathrm{o}} = 1.02$ kW ($P_{\mathrm{o}} = 0.6$). As the power is increased to 1.7 kW, the efficiency decreases to 97.89%. At the lowest load conditions, with $p_{\mathrm{o}} = 85$ W ($P_{\mathrm{o}} = 0.05$), the

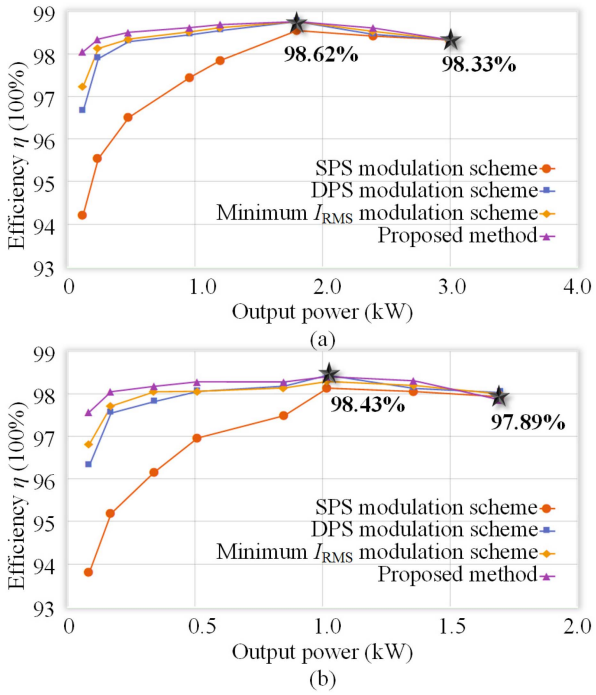

Fig. 18. Efficiency curves of the DAB prototype in different voltage gain and power flow conditions under different modulation scheme methods. (a) V_{in} = 240 V, V_o = 504 V (M = 1.4). (b) V_{in} = 240 V, V_o = 216 V (M = 0.6).

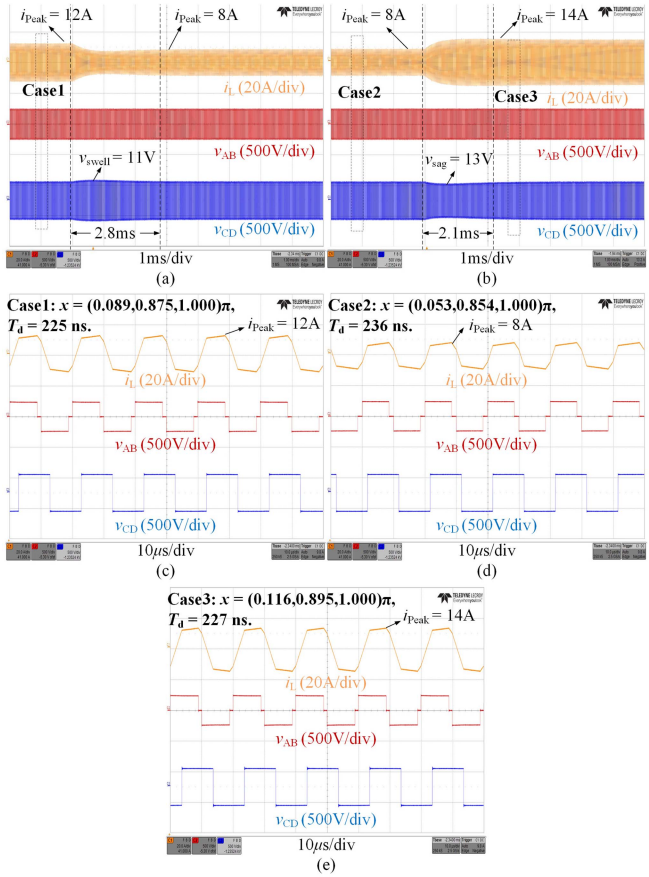

Fig. 19. (a) Overview of the operation waveforms in R_L = 60 Ω (P_o = 1.5 kW) to R_L = 100 Ω (P_o = 0.9 kW) load step-down condition. (b) Overview of the operation waveforms in R_L = 100 Ω (P_o = 0.9 kW) to R_L = 50 Ω (P_o = 1.8 kW) load step-up condition. (c) Zoomed waveform in case1 when R_L = 60 Ω with x = (0.089, 0.875, 1.000)π, T_d = 225 ns. (d) Zoomed waveform in case2 when R_L = 100 Ω with x = (0.053, 0.854, 1.000)π, T_d = 236 ns. (e) Zoomed waveform in case3 when R_L = 50 Ω with x = (0.116, 0.895, 1.000)π, T_d = 227 ns.

SPS modulation scheme yields an efficiency of 93.79%, while the proposed method maintains a high efficiency of 97.54%.

Comparatively, the efficiency curve for V_o = 216 V is slightly lower than that for V_o = 504 V. This discrepancy can be attributed to the fact that V_o = 216 V deviates significantly from the rated output voltage and operates at a lower power base value. Analysis of Fig. 18 reveals that as the load decreases, the efficiency gap between the proposed method and other approaches becomes more pronounced. The SPS modulation scheme demonstrates reduced efficiency, primarily due to the absence of ZVS and an increase in P_{Cond}. In contrast, the DPS modulation scheme achieves higher efficiency through a simplified control method. The minimum I_{rms} modulation scheme, however, falls short in attaining full ZVS during light load conditions, mainly due to its neglect of dead time and power MOSFET parasitic capacitors.

Fig. 19 illustrates the closed-loop experimental waveforms observed during load step changes. The load resistor R_L is ascertained by measuring the output voltage V_o and current I_o. Consequently, the output power p_o is computed from V_o and I_o. The corresponding P_o is calculated based on the base voltage value in this condition. In these experiments, one ITECH IT6012B-800-50 regenerative power source is employed as the input voltage source while another one is served as the electrical dc load. During the load step change test, the input voltage is maintained constantly at 240 V. The output voltage reference is set at V_{ref} = 300 V, while the load resistance is adjusted using the electrical dc load.

In the load step-down scenario, R_L is shifted from 60 Ω (p_o = 1.5 kW) to 100 Ω (p_o = 0.9 kW), with a transition duration of 2.8 ms and an accompanying voltage swell of 11 V. Conversely, for the step-up condition, R_L shifts from 100 Ω (p_o = 0.9 kW) to 50 Ω (p_o = 1.8 kW), with a 2.1 ms transition and a 13 V voltage sag. The zoomed stable state operation waveforms are shown from Fig. 19(c)–(e). In these instances, the optimal control parameters are identified as x = (0.089,0.875,1.000)π, T_d = 225 ns, x = (0.053,0.854,1.000)π, T_d = 236 ns, and x = (0.116,0.895,1.000)π, T_d = 227 ns, respectively. The peak inductor currents recorded are 12, 8, and 14 A, respectively. These experimental findings corroborate the efficacy of the proposed method in achieving stable and seamless output during step load changes, without any dc bias in the inductor current throughout the transitions.

Among the various modulation schemes, the proposed method consistently achieves the highest efficiency, whether in voltage gain step-up or step-down conditions. This trend holds true for scenarios involving power backflow conditions as well, owing to the symmetric characteristics of the DAB converters. A comparison between the proposed method and existing approaches is succinctly presented in Table IV. In the case of traditional SPS, DPS, and TPS modulation schemes [1], [2], [14], [15], [16], [17], [18], [14], [19], [20], [21], [22],

TABLE IV
COMPARISON OF DIFFERENT METHODS

Methods	Advantage	Disadvantage
SPS [1], [2]	1) Simple calculation. 2) High efficiency in rated condition.	1) Analysis based on ideal, lossless mode. 2) Low efficiency in light load condition.
DPS [15], [16], [17] EPS [14], [18], [14]	1) Easy to use. 2) Improved efficiency in light load conditions.	1) Analysis based on ideal, lossless mode. 2) Unable to achieve ZVS in light load condition.
TPS, minimum I_{rms} modulation scheme [19], [20], [21], [22]	1) Complex to use. 2) Improved efficiency in light load conditions.	1) Analysis based on ideal, lossless mode. 2) Unable to achieve ZVS in light load condition.
[23], [24], [25]	Consider the impact of deadtime and parasitic capacitor.	* [23] and [25] only considered the SPS case. [24] only considered the EPS case.
This work	**1) Consider the impact of deadtime and parasitic capacitor. 2) The optimal control parameter is proposed.**	**Time-consuming in the experimental data-driven process.**

* These analyses solely addressed specific conditions. Expanding these analyses to encompass TPS modulation schemes becomes challenging due to the abundance of potential combinations and equivalent stages.

their analyses frequently rely on an idealized, lossless DAB model. Consequently, inaccuracies may arise in voltage gain, power flow, and steady-state waveforms. While some studies have considered deadtime and parasitic components [23], [24], [25], their focus remains primarily on typical operating scenarios. Expanding these analyses to encompass broader TPS modulation schemes introduces a complex array of potential combinations and equivalent configurations. Given that most of the existing literature is based on simplified equivalent models, it becomes challenging to ascertain optimal control parameters suitable for all operational conditions, spanning both step-up and step-down scenarios, as well as forward and backward power flow conditions.

Regarding the proposed method, we employed a hybrid data-driven model that combines insights derived from both simulation and practical experimentation. Notably, the experimental data utilized in this approach is gathered from the experimental prototype, thus inherently factoring in considerations for deadtime and parasitic components. One drawback of the proposed method, however, is its relatively time-consuming data acquisition process during experimentation when compared to conventional methods.

IV. DISCUSSION

Beyond power loss minimization, various AI methodologies have found application in power electronics. For scenarios where rapid dynamic response is a critical factor, methods based on conventional PI controllers exhibit superior efficacy. On the other hand, in contexts where the emphasis is on augmenting steady-state performance, or where the need for dynamic responsiveness is not as pronounced, the approach proposed in this study offers greater suitability.

In future research efforts, we aim to accelerate the methodologies underpinning simulation and experimental data acquisition. This strategy inherently involves a balance between data quality and quantity, and the accuracy of the data-driven model. Resolving this balance is a key focus for subsequent studies. At present, the deployment of our proposed methodology is notably time-consuming. Another important area for forthcoming research is the strategic utilization of this data-driven model to achieve real-time control optimization in power converters.

V. CONCLUSION

This article presents an innovative hybrid data-driven model for minimizing power losses in DAB converter, effectively merging insights from both simulation and experimentation. The divergence between experimental and simulated models is encapsulated within a residual branch, which plays a key role in the optimization process for obtaining optimal control parameters. By meticulously scrutinizing outcomes derived from experiments carried out on a 3-kW DAB prototype, we deploy a perturbation-based optimal examination approach to validate the credibility and effectiveness of the proposed efficiency optimization methodology.

REFERENCES

[1] R. W. DeDoncker, D. M. Divan, and M. H. Kheraluwala, "A three-phase soft-switched high power density DC-to-DC converter for high power applications," *IEEE Trans. Ind. Appl.*, vol. 27, no. 1, pp. 63–73, Jan./Feb. 1991.

[2] M. H. Kheraluwala, R. W. Gascoigne, D. M. Divan, and E. D. Baumann, "Performance characterization of a high-power dual active bridge DC-to-DC converter," *IEEE Trans. Ind. Appl.*, vol. 28, no. 6, pp. 1294–1301, Nov./Dec. 1992.

[3] B. Zhao, Q. Song, J. Li, W. Liu, G. Liu, and Y. Zhao, "High-frequency-link DC transformer based on switched capacitor for medium-voltage DC power distribution application," *IEEE Trans. Power Electron.*, vol. 31, no. 7, pp. 4766–4777, Jul. 2016.

[4] Z. Zhang, Y.-Y. Cai, Y. Zhang, D.-J. Gu, and Y.-F. Liu, "A distributed architecture based on microbank modules with self-reconfiguration control to improve the energy efficiency in the battery energy storage system," *IEEE Trans. Power Electron.*, vol. 31, no. 1, pp. 304–317, Jan. 2016.

[5] Z. Xiao, L. Zhang, Z. He, and Y. Tang, "Efficiency improvement of DAB converters with enhanced inductor current classification," in *Proc. IEEE Energy Convers. Congr. Expo.*, 2023, pp. 2631–2638.

[6] B. Zhao, Q. Song, and W. Liu, "A practical solution of high-frequency-link bidirectional solid-state transformer based on advanced components in hybrid microgrid," *IEEE Trans. Ind. Electron.*, vol. 62, no. 7, pp. 4587–4597, Jul. 2015.

[7] Q. Ye, R. Mo, and H. Li, "Low-frequency resonance suppression of a dual-active-bridge DC/DC converter enabled DC microgrid," *IEEE J. Emerg. Sel. Topics Power Electron.*, vol. 5, no. 3, pp. 982–994, Sep. 2017.

[8] L. Wang, D. Zhang, Y. Wang, B. Wu, and H. S. Athab, "Power and voltage balance control of a novel three-phase solid-state transformer using multilevel cascaded H-bridge inverters for microgrid applications," *IEEE Trans. Power Electron.*, vol. 31, no. 4, pp. 3289–3301, Apr. 2016.

[9] F. Krismer and J. W. Kolar, "Accurate small-signal model for the digital control of an automotive bidirectional dual active bridge," *IEEE Trans. Power Electron.*, vol. 24, no. 12, pp. 2756–2768, Dec. 2009.

[10] F. Krismer and J. W. Kolar, "Efficiency-optimized high-current dual active bridge converter for automotive applications," *IEEE Trans. Ind. Electron.*, vol. 59, no. 7, pp. 2745–2760, Jul. 2012.

[11] J. Everts, F. Krismer, J. Van den Keybus, J. Driesen, and J. W. Kolar, "Optimal ZVS modulation of single-phase single-stage bidirectional DAB AC–DC converters," *IEEE Trans. Power Electron.*, vol. 29, no. 8, pp. 3954–3970, Aug. 2014.

[12] T. Zhao, G. Wang, S. Bhattacharya, and A. Q. Huang, "Voltage and power balance control for a cascaded H-bridge converter-based solid-state transformer," *IEEE Trans. Power Electron.*, vol. 28, no. 4, pp. 1523–1532, Apr. 2013.

[13] J. Liu, J. Yang, J. Zhang, Z. Nan, and Q. Zheng, "Voltage balance control based on dual active bridge DC/DC converters in a power electronic traction transformer," *IEEE Trans. Power Electron.*, vol. 33, no. 2, pp. 1696–1714, Feb. 2018.
[14] H. Shi et al., "Minimum-backflow-power scheme of DAB-based solid-state transformer with extended-phase-shift control," *IEEE Trans. Ind. Appl.*, vol. 54, no. 4, pp. 3483–3496, Jul./Aug. 2018.
[15] H. Bai and C. Mi, "Eliminate reactive power and increase system efficiency of isolated bidirectional dual-active-bridge DC–DC converters using novel dual-phase-shift control," *IEEE Trans. Power Electron.*, vol. 23, no. 6, pp. 2905–2914, Nov. 2008.
[16] B. Zhao, Q. Song, and W. Liu, "Power characterization of isolated bidirectional dual-active-bridge DC–DC converter with dual-phase-shift control," *IEEE Trans. Power Electron.*, vol. 27, no. 9, pp. 4172–4176, Sep. 2012.
[17] B. Zhao, Q. Song, and W. Liu, "Efficiency characterization and optimization of isolated bidirectional DC–DC converter based on dual-phase-shift control for DC distribution application," *IEEE Trans. Power Electron.*, vol. 28, no. 4, pp. 1711–1727, Apr. 2013.
[18] B. Zhao, Q. Yu, and W. Sun, "Extended-phase-shift control of isolated bidirectional DC–DC converter for power distribution in microgrid," *IEEE Trans. Power Electron.*, vol. 27, no. 11, pp. 4667–4680, Nov. 2012.
[19] J. Huang, Y. Wang, Z. Li, and W. Lei, "Unified triple-phase-shift control to minimize current stress and achieve full soft-switching of isolated bidirectional DC–DC converter," *IEEE Trans. Ind. Electron.*, vol. 63, no. 7, pp. 4169–4179, Jul. 2016.
[20] Z. Xiao, Z. He, H. Wang, A. Luo, Z. Shuai, and J. M. Guerrero, "General high-frequency-link analysis and application of dual active bridge converters," *IEEE Trans. Power Electron.*, vol. 35, no. 8, pp. 8673–8688, Aug. 2020.
[21] Z. Xiao, Z. He, Z. Li, L. Zhu, and L. Wang, " Unified description and optimization method of dual active bridge DC-DC converters," *IEEE Trans. Power Electron.*, vol. 37, no. 10, pp. 11839–11854, Oct. 2022.
[22] F. Krismer and J. W. Kolar, "Closed form solution for minimum conduction loss modulation of DAB converters," *IEEE Trans. Power Electron.*, vol. 27, no. 1, pp. 174–188, Jan. 2012.
[23] Y. Xie, J. Sun, and J. S. Freudenberg, "Power flow characterization of a bidirectional galvanically isolated high-power DC/DC converter over a wide operating range," *IEEE Trans. Power Electron.*, vol. 25, no. 1, pp. 54–66, Jan. 2010.
[24] H. Shi, H. Wen, and Y. Hu, "Deadband effect and accurate ZVS boundaries of GaN-based dual-active-bridge converters with multiple-phase-shift control," *IEEE Trans. Power Electron.*, vol. 35, no. 9, pp. 9886–9903, Sep. 2020.
[25] B. Zhao, Q. Song, W. Liu, and Y. Sun, "Dead-time effect of the high-frequency isolated bidirectional full-bridge DC–DC converter: Comprehensive theoretical analysis and experimental verification," *IEEE Trans. Power Electron.*, vol. 29, no. 4, pp. 1667–1680, Apr. 2014.
[26] Z. Xiao, Y. Jiang, T. Sun, Y. Wu, and Y. Tang, "Refining power converter loss evaluation: A transfer learning approach," *IEEE Trans. Power Electron.*, vol. 39, no. 4, pp. 4313–4324, Apr. 2024, doi: 10.1109/TPEL.2023.3349178.
[27] Y. Tang et al., "Reinforcement learning based efficiency optimization scheme for the DAB DC–DC converter with triple-phase-shift modulation," *IEEE Trans. Ind. Electron.*, vol. 68, no. 8, pp. 7350–7361, Aug. 2021.
[28] F. Lin et al., "AI-based design with data trimming for hybrid phase shift modulation for minimum-current-stress dual active bridge converter," *IEEE J. Emerg. Sel. Topics Power Electron.*, to be published, doi: 10.1109/JESTPE.2022.3232534.

Ziheng Xiao (Member, IEEE) received the B.S. degree in electrical engineering and automation and the Ph.D. degree in electrical engineering from the College of Electrical and Information Engineering, Hunan University, Changsha, China, in 2017 and 2022, respectively.

Since 2022, he has been a Research Fellow with Energy Research Institute, Nanyang Technological University, Singapore. His main research interests include the medium voltage dc system, dual active bridge converters, resonant converters, energy router, and the application of artificial intelligence in power electronics.

Dr. Xiao was the Session chair for the 49th Annual Conference of the IEEE Industrial Electronics Society.

Yu Jiang received the B.S. degree in electrical engineering and automation and the Ph.D. degree in control theory and control engineering from the College of Electrical and Information Engineering, Hunan University, Changsha, China, in 2017 and 2023, respectively.

Since 2023, she has been a Research Fellow with the Chinese University of Hong Kong, Hong Kong. Her research interests include nonlinear analysis, chaos theory, pattern recognition, and machine learning for industrial process applications.

Zhigang Yao received the B.Sc. and Ph.D. degrees in electrical engineering from Chongqing University, Chongqing, China, in 2014 and 2020, respectively.

He was with the School of Electrical Engineering, Southwest Jiaotong University, Chengdu, China, as an Assistant Professor in 2020. Since 2022, he has been a Research Fellow with Nanyang Technological University, Singapore. His current research interests include interleaving techniques, high power density dc–dc converters, grid-connected inverters, and renewable energy systems.

Zhou He (Graduate Student Member, IEEE) received the B.S. degree in electrical engineering from Hebei University of Technology, Tianjin, China, in 2018. He is currently working toward the Ph.D. degree in electrical engineering with the School of Electrical and Electronic Engineering, Huazhong University of Science and Technology, Wuhan, China.

From 2022 to 2023, he was a Visiting Ph.D. Student with Nanyang Technological University, Singapore. His research interests include multilevel converters, soft-switching converters, applications of wide-bandgap power electronic devices, and pulsed power technology.

Yongbin Jiang (Member, IEEE) received the B.S. degree in electrical automatization from Jiangsu University, Zhenjiang, China, in 2012, and the M.S. degree in instrument science and technology and the Ph.D. degree in electrical engineering from Xi'an Jiaotong University, Xi'an, China, in 2016 and 2020, respectively.

From 2020 to 2022, he was the Director with the Digital Energy Laboratory, UNISOC (Shanghai) Technologies Company Ltd., Shanghai, China. Since 2022, he has been a Research Fellow with Nanyang Technological University, Singapore. He has authored and coauthored one ESI highly cited paper. His research interests include wireless power transfer, high frequency and high power density dc/dc converters, signal processing, and digital control technology.

Dr. Jiang was a recipient of the Best Paper Award of IEEE 10th International Symposium on Power Electronics for Distributed Generation Systems in 2019 and the Best ECCE Paper on Emerging Technology Award from IEEE Power Electronics Society in 2020.

Yaohua Li received the B.Eng. degree in electrical engineering from the University of Calgary, Calgary, Canada, in 2020, and the M.Sc. degree in power engineering in 2021 from Nanyang Technological University, Singapore, where he is currently working toward the Ph.D. degree in electrical engineering.

His research interests include wireless power transfer, high-frequency magnetics, and artificial intelligence.

Yi Tang (Senior Member, IEEE) received the B.Eng. degree in electrical engineering from Wuhan University, Wuhan, China, in 2007, the M.Sc. degree in power electronics and power drives, and the Ph.D. degree in electrical engineering from the School of Electrical and Electronic Engineering, Nanyang Technological University, Singapore, in 2008 and 2011, respectively.

From 2011 to 2013, he was a Senior Application Engineer with Infineon Technologies Asia Pacific, Singapore. From 2013 to 2015, he was a Postdoctoral Research Fellow with Aalborg University, Aalborg, Denmark. Since 2015, he has been with Nanyang Technological University, Singapore, where he is currently a tenured Associate Professor. His research interests include power electronics and its applications in smart grid and e-mobility systems.

Dr. Tang was a recipient of the Infineon Top Inventor Award in 2012, the Early Career Teaching Excellence Award in 2017, and four IEEE Prize Paper Awards. He is an Associate Editor for the IEEE TRANSACTIONS ON POWER ELECTRONICS and the IEEE JOURNAL OF EMERGING AND SELECTED TOPICS IN POWER ELECTRONICS.